Chapter 20
Water-Content Electrical Property Tomography (wEPT) for Mapping Brain Tissue Conductivity in the 200–1000 kHz Range: Results of an Animal Study

Cornelia Wenger, Hadas Sara Hershkovich, Catherine Tempel-Brami, Moshe Giladi, and Ze'ev Bomzon

20.1 Introduction and Motivation

Methods for non-invasively imaging the electrical properties (EPs) of tissues in vivo have been a recent topic of significant interest. Specifically, many research groups have attempted to create volumetric images of electrical conductivity (σ) and relative permittivity (ε_r) at specific frequencies. These studies have been motivated by a number of reasons, the primary one being that the interaction between applied electromagnetic fields and biological tissue is determined by their EPs [1]. Thus, non-invasively imaging EPs within the body offers important insight for a variety of clinical applications.

One example is the safety studies concerned with understanding tissue heating that occurs during high-field MRI applications [2–5]. The calculation of the local specific absorption rate (SAR) of tissue requires knowledge of the electric field induced by radiofrequency excitation and the local EPs of tissues [4]. And as summarized in [3], the actual local SAR pattern varies significantly with patient size and position, as well as patient-specific EPs. Antenna design for wearable and implantable medical devices is another high-frequency application that would benefit from knowledge of the patient-specific EP distribution [6]. And virtual human models are often used to estimate induced electric fields, which would benefit from individual and frequency-dependent EP maps [6]. Major low frequency medical applications which are being studied with computational models include neurostimulation techniques (such as TMS [7] or tDCS [8]) or MEG/EEF source detection studies. In all of these studies, knowledge of the spatial distribution of the induced electric field is necessary to interpret experimental results and to optimize field delivery [9].

C. Wenger (✉)
Novocure GmbH, Lucerne, Switzerland
e-mail: cwenger@novocure.com

H. S. Hershkovich · C. Tempel-Brami · M. Giladi · Z. Bomzon
Novocure Ltd, Haifa, Israel

S. Makarov et al. (eds.), *Brain and Human Body Modeling*,
https://doi.org/10.1007/978-3-030-21293-3_20

Therefore, a method for rapidly creating accurate and patient-specific EP maps would be important for future improvement of these medical applications.

Furthermore, experimental measurements have revealed that the EPs of pathological tissues often differ from those of healthy tissues, with generally higher σ and ε_r values in cancerous tissue at both low and high frequencies [10–16]. The authors associate the EP difference with the changes in water content that occur in neoplastic tissue, which are due to varying protein hydration, vascularization, alterations in membrane permeability and amount of extracellular fluid, as well as packing density, and cancer cell orientation. Thus, mapping EPs may help to detect malignant regions with higher sensitivity than current imaging techniques. This knowledge contributes to further development and treatment planning of medical applications such as radiofrequency tissue ablation, electro-chemotherapy and gene therapy with reversible electroporation, nanoscale pulsing, and irreversible electroporation, as described and summarized in [16, 17].

Another example, and the motivation for this study, is a cancer treatment modality called Tumor Treating Fields (TTFields). TTFields are an antimitotic cancer treatment using alternating electric fields with intermediate frequencies (between 100 and 300 kHz) and low intensities (between 1 and 3 V/cm) to disrupt cell division in tumors [18, 19]. TTFields are FDA approved as a monotherapy for recurrent glioblastoma [20] and as a combination therapy with chemotherapy for newly diagnosed glioblastoma patients [21]. TTFields treatment of glioblastoma is performed with the Optune™ device, which delivers alternating electric fields at a frequency of 200 kHz via two pairs of transducer arrays [22, 23]. Since TTFields treatment efficacy depends on delivered field intensity at the target, patient-specific treatment planning [24] provides array layouts with personalized locations of transducers to optimize induced field intensity in the tumor. Several computational modeling studies have used realistic computational head models to study the induced electric field distribution during Optune™ treatment [25–27]. These studies all showed that the field intensity delivered to the tumor is dependent on the dielectric properties, specifically the electric conductivity σ of the healthy and pathological tissues of the patient's brain [26, 28, 29]. These computational studies usually assume homogenous and isotropic EPs in different tissue types, which is a reasonable assumption for well-studied healthy brain tissues like the gray matter (GM), white matter (WM), and cerebrospinal fluid (CSF) [30, 31]. Yet, the glioblastoma tumor area is typically a very heterogeneous region composed of enhancing or non-enhancing parts, and cystic or necrotic compartments. Furthermore, EP measurements of cancerous tissue also predict higher patient variability compared to healthy tissue (e.g [32]). Thus, a patient-specific EP map of the brain would be optimal to accurately evaluate the induced electric field distribution and intensities at the tumor bed. For a detailed review on preclinical, clinical, and modeling studies related to TTFields, see [33].

A variety of different approaches have been proposed to non-invasively image EPs of biological tissue at different frequencies over the past two decades. The oldest methods for mapping EPs in a volume include electrical impedance tomography [34] and magnetic induction tomography [35]. These techniques suffer from the inherently ill-posedness of the inverse problem, leading to low resolution, low

sensitivity, and limited applicability in the clinic. Other attempts to obtain EP maps with high spatial resolution include magnetic resonance electrical impedance tomography (MREIT) [36], as well as other (magneto-) acoustic methods. MREIT was proposed to perform conductivity imaging at DC using the MR current density imaging approach [37]. According to [38], it remains a technical problem to reduce current injection down to a level for routine clinical use while maintaining the spatial resolution of the resulting conductivity image without long imaging sequences. More recently, in an attempt to overcome the limitations of these techniques, MR-based electrical properties tomography (EPT) was introduced by Haacke et al. [39]. EPT is based on B_1 mapping, i.e., the EPs are reconstructed from measurable RF-coil-induced magnetic fields (B_1 fields) by employing Maxwell's equation. The EPT approach has been well studied and a comprehensive review can be found in [40]. However, a recent study [41] points out certain challenges associated with EPT, including boundary reconstruction errors due to the fact that the Helmholtz equation does not hold at regions where tissue types coexist and the high degree of symmetry that is needed to obtain higher signal-to-noise ratio.

The authors of this study propose a new, alternative approach termed water-content-based electrical properties tomography (wEPT) [41]. wEPT utilizes two T1-MR images to map σ and ε_r within tissue. The foundation for wEPT is Maxwell's mixture theory, which suggests that tissue conductivity is highly correlated with water content, which in turn can be estimated from the ratio between two T1-weighted MR images with different repetition times (TR). wEPT has been used to map brain conductivity at 128 MHz without concern about inhomogeneity among tissues. Because wEPT mapping is based on relatively standard and rapid MRI imaging sequences, it is a highly attractive approach for implementation in research and in the clinic.

Having TTFields treatment of glioblastoma patients in mind, the aims of this study were

(a) To test whether wEPT can be applied to the frequency range of 200–1000 kHz
(b) To establish that wEPT can be used to map σ of healthy brain tissue in this frequency range
(c) To investigate whether or not wEPT can be used to map EPs in brain tumors

To achieve these goals, a series of experiments was performed utilizing BSA phantoms, samples of calf brain and in vivo experiments in tumor bearing-rats. A detailed description of the experiments and their results follow.

20.2 Methods and Results

This section starts with a summary of the theoretical basis behind the wEPT approach (Sect. 20.2.1).

In order to address our above-stated aims, the study was performed in three stages. Materials and methods as well as obtained results will be presented in

chronological order of experiments: First the feasibility of applying wEPT at 200 kHz was established by performing wEPT measurements on phantoms (Sect. 20.2.2). Then, wEPT was applied to estimate the EPs of healthy brain tissue derived from calf brains (Sect. 20.2.3). Finally, we tested the applicability of wEPT to map σ in tumor tissue derived from tumor bearing-rats (Sect. 20.2.4).

All imaging was performed on an in-house Bruker ICON 1.0 T MRI machine. Animal experiments were approved by the Israeli Animal Care.

20.2.1 Theory of wEPT

The specific EPs of a tissue are determined by relative intra- and extracellular volumes, membrane permeability, ion concentration, and mobility [15]. During studies of the dielectric properties of various types of tumor and normal tissues with varying water content, it has been demonstrated that their EPs conform to the Maxwell mixture theory for high and low water-content tissues [42–44]. Since cell membranes have low impedance at RF frequencies, the EPs of a tissue become highly correlated with the water fraction. It has been reported that the tissues' conductivity at these frequencies is mostly determined by the ionic conductivity of cytoplasm and that the permittivity is likely determined by the water fraction [45]. For ultra-high frequencies, the EPs are almost entirely determined by the water content due to the polarization of polar media-like water [15, 42].

Thus, the wEPT approach assumes that at an imaging frequency of 128 MHz, the electrical conductivity σ and the relative permittivity ε_r can be modeled as a monotonic function of tissue water content (WC) under the principle of Maxwell's mixture theory. The wEPT approach seeks to circumvent the need for lengthy imaging processes by computing the WC maps using a transfer function derived from the image ratio (IR) of two T1-weighted images with different repetition times (TR) via

$$\mathrm{WC} = w_1 e^{-w_2 \mathrm{IR}} \tag{20.1}$$

where w_1 and w_2 are determined through curve fitting.

The image ratio assumption is based on the fact that both properties, the WC and the IR, can be expressed as functions of the T_1 relaxation values (T1). On the one hand, early works had already demonstrated that the WC can be directly related to the T1 value in living tissue [46]. On the other hand, the IR can be expressed by

$$\mathrm{IR} = \kappa \left(\frac{1 - e^{-\mathrm{TR_s}/\mathrm{T_1}}}{1 - \cos\theta_1 \cos 2\theta_1 e^{-\mathrm{TR_s}/\mathrm{T_1}}} \right) / \left(\frac{1 - e^{-\mathrm{TR_l}/\mathrm{T_1}}}{1 - \cos\theta_1 \cos 2\theta_1 e^{-\mathrm{TR_l}/\mathrm{T_1}}} \right),$$

where θ_1 and $\theta_2$are the nominal angles of the excitation and refocusing pulses, κ is a factor compensating signal gain fluctuations, and $\mathrm{TR_s}$ and $\mathrm{TR_l}$ are the short and long repetition times of the two images, respectively.

In order to connect WC and the EPs of brain tissues, the authors in [41] used landmark points for the three primary brain tissues (GM, WM, and CSF) and gathered corresponding values for WC, σ, and ε from an extensive literature search. Two separate curve fitting procedures revealed the best fit for a monotonically increasing function between WC and the EPs at 128 MHz:

$$\sigma = c_1 + c_2 e^{c_3 \mathrm{WC}} \tag{20.2a}$$

$$\varepsilon = p_1 \mathrm{WC}^2 + p_2 \mathrm{WC} + p_3 \tag{20.2b}$$

In order to find appropriate values for short and long repetition times, the authors in [41] plotted IR as a function of T1 with different combinations of TR_s and TR_l and assuming $\theta_1 = 90^\circ$, $\theta_2 = 180^\circ$, and $\kappa = 1$. The preferred combination was determined by the largest IR signal and greatest difference between the WM with the highest T1 and the CSF with the lowest T1. In the original study, TR_s=700 ms and TR_l=3000 ms were considered.

20.2.2 BSA Phantom

We initially conducted a phantom study to test the feasibility of performing wEPT studies for a lower frequency of 200 kHz. The phantom was created by placing different solutions of BSA (bovine serum albumin) in DPBS (Dulbecco's phosphate-buffered saline) into a plastic plate with cylindrical chambers. Each chamber was filled with solutions of varying concentrations of albumin (20%, 25%, 30%, and 40%). In order to obtain the coefficients of the wEPT model equations, we measured four parameters of the BSA solutions at 200 kHz: T1, WC, σ, and ε_r (Table 20.1). The T1 value of the solutions was estimated using the variable TR method, in which the T1 value is estimated from exponential curve fitting of the signal intensity in a voxel for a selection of spin-echo images with varying TR_s (compare Fig. 20.1b). The WC of the solutions can be deduced from the known

Table 20.1 BSA experiment

	BSA20	BSA25	BSA30	BSA40
T1 *measured*	1119.4	928.0	741.0	483.2
WC *measured*	79%	75%	70%	60%
WC *wEPT*	80%	75%	70%	60%
σ *measured*	0.90	0.79	0.69	0.49
σ *wEPT*	0.88	0.79	0.69	0.49
ε *measured*	315.60	284.89	277.17	262.51
ε *wEPT*	300.44	284.94	277.20	261.92

Measured and wEPT-estimated values of T1 (ms), WC (%), σ (S/m), and ε_r at 200 kHz for four BSA solutions

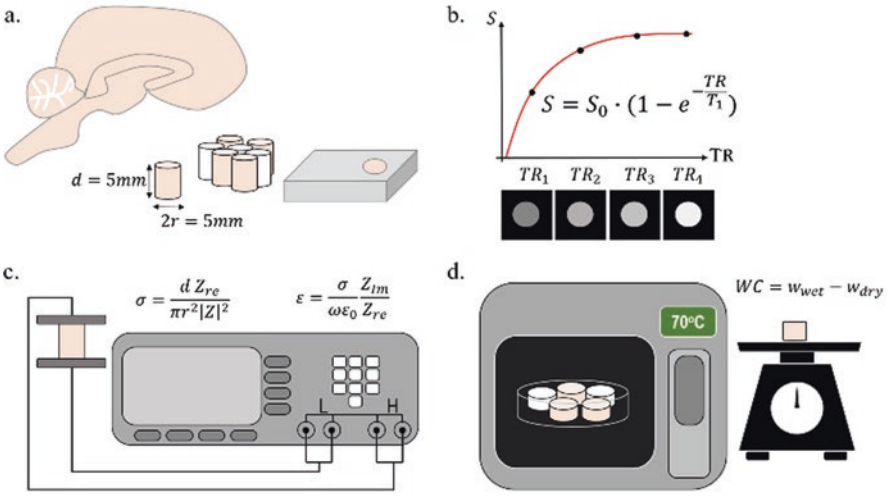

Fig. 20.1 Experimental setup of brain tissue measurements. (**a**) GM and WM sample preparation (**b**) T1 values were estimated with the variable TR method. (**c**) An LCR meter was used to estimate σ and ε for frequencies between 20 Hz and 1 MHz. (**d**) WC is estimated as the difference between the weight of wet and dry tissue samples

concentration of albumin in each solution. The EPs of the solutions were measured utilizing the parallel-plates method with a cylindrical chamber (10 mm diameter, 9 mm thickness) sandwiched between two Ag/AgCl electrodes, which were connected to an LCR meter (Keysight E4980AL). Sample impedance was measured in the range of 20 Hz to 1 MHz, and σ and ε_r were derived from these measurements using a well-established procedure. By testing different combinations of 13 spin-echo images with TR ranging from 50 ms to 5 s, we found that a combination of TR_s/TR_l=700/4000 yields optimal distinction of IR values between the BSA solutions tested. Furthermore, a few different curve-fitting methods were tested for mapping EPs at 200 kHz from WC (including polynomial and exponential fitting), which all yielded similar wEPT estimations. Table 20.1 summarizes experimentally measured values of T1, WC, σ, and ε at 200 kHz, as well as the estimated values with wEPT, which are the mean values of the properties in the central ROIs. Obtained results predict that wEPT estimations of the WC and EPs in all solutions match very well with corresponding measurements. Only minor discrepancies are found for the BSA 20% solution with the highest WC.

20.2.3 Calf Brain Samples

In order to establish a wEPT model for mapping brain tissue EPs at 200 kHz, appropriate coefficients have to be found via curve fitting experimental measurements to Eqs. 20.1, 20.2a, and 20.2b. Thus, measurements of T1, WC, σ, and ε were

performed for three tissue types: GM, WM, and CSF. The first experiments with brain tissue were conducted with excised samples of three calf brains received 48–72 hours postmortem. Although there was some uncertainty about storage and handling of the first bovine brains prior to delivery, we wanted to establish a workflow for experimental procedures and refine our planned methodology.

For sample preparation, the brain was cut using tweezers to expose the thalamus where cylindrical samples of GM were punched out. Cylindrical WM samples were punched out of thick coronal slices. Different punches with diameters ranging from 5 to 7 mm were used, depending on the operator and the brain region. The samples were placed in a 5 mm thick polycarbonate plate with holes of 5 mm diameter, and were sealed with cellophane (Fig. 20.1a).

To estimate T1, plates containing up to eight samples were placed in the MRI to acquire spin-echo images with variable TR_s (Fig. 20.1b). Samples were initially kept about 2 mm thicker than the plates to ensure good image quality. The plates were moved to the LCR measurement station after MRI image acquisition (Fig. 20.1c). The cover of each sample was removed just before measurement, when it was cut to the plate thickness of 5 mm. While assuring full contact, the Ag/AgCl electrodes were placed on the top and bottom of each tissue sample. The LCR meter was used to record the impedance of each sample for a frequency sweep between 20 Hz and 1 MHz, at a lab temperature of about 21 °C. σ and ε values were derived from the impedance measurements assuming a parallel plate measurement system geometry.

The WC of the samples was defined as the weight difference between wet and dry tissue samples. After the LCR measurement, the samples were transferred to a pre-weighted weighing paper. The gross weight of sample and paper was documented with a scale (ME104 Metler Toledo SN004) prior to and then after placing them in an oven at 70 °C for 48 h of drying (Fig. 20.1d). A preliminary experiment assured that the weight of the paper is not affected by the drying process.

Using this process, measurements of T1, WC, σ, ε of 32 different calf brain samples (16 WM, 13 GM, 3 mixed samples) were obtained. For model completion, two porcine CSF samples were also measured. In order to implement wEPT on these samples, T_1-weighted images with $TR_s = 700$ ms and $TR_l = 3000$ ms were chosen for calculating IR. IR was plotted against the measured WC of all 34 tissue samples, and coefficients w_1 and w_2 in Eq. 20.1 were found via curve fitting (Fig. 20.2a). Subsequently, the same procedure was performed for equations that relate the WC to the EPs (Eqs. 20.2a and 20.2b). We created two sets of σ coefficients c_1, c_2, c_3 and ε_r coefficients p_1, p_2, p_3. One set of coefficients was for a frequency of 200 kHz (Fig. 20.2b, c); the second set was for the highest measured frequency of 1 MHz (data not shown).

The following procedure was used to analyze the wEPT model of the bovine brain samples and estimate EPs at 200 kHz and 1 MHz: IR was calculated for each voxel in the sample, corresponding WC values are calculated via Eq. 20.1 and EP values with Eqs. 20.2a and 20.2b. The estimated properties were averaged over the sample volume to yield the average IR, WC, and EPs of each sample, which were compared to the measured values (compare Table 20.2). Figure 20.3 illustrates the

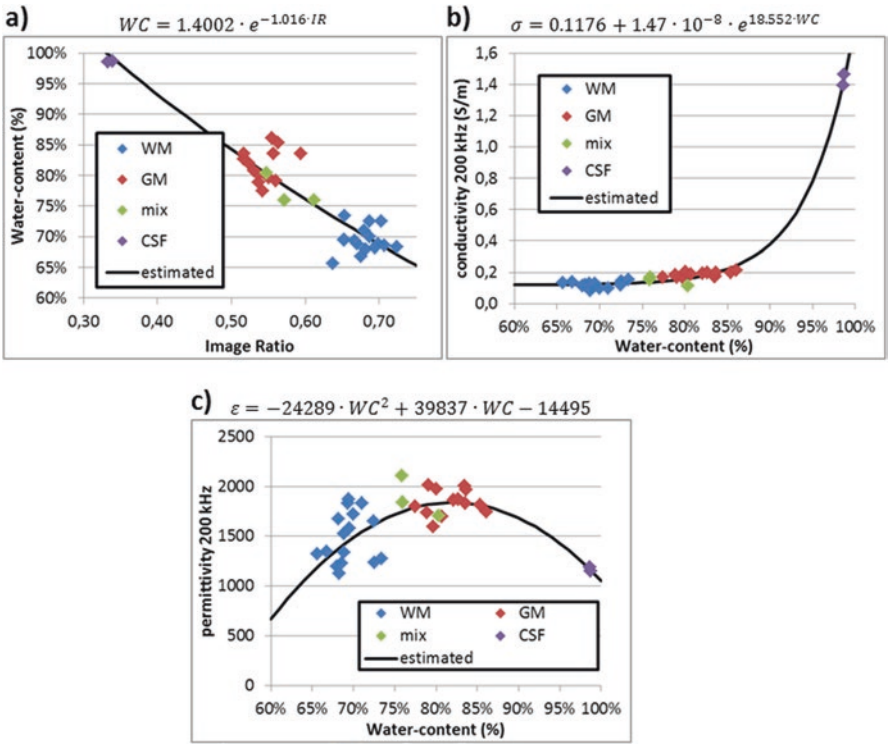

Fig. 20.2 wEPT model creation for brain tissue of calves1–3, for WM (blue), GM (red), mixed samples (green), and pig CSF (purple). Model coefficients were obtained by curve fitting for mapping WC from IR with Eq. 20.1 (**a**), for σ mapping with Eq. 20.2a (**b**), and ε_r mapping with Eq. 20.2b (**c**). The equations with their coefficients are listed above each panel

Table 20.2 Average relative error of wEPT estimates in all brain samples of calves 1–3 compared to measured values

	IR (%)	WC (%)	σ^{200kHz} (%)	σ^{1MHz} (%)	ε^{200kHz} (%)	ε^{1MHz} (%)
mod_a1	1.3	3.8	14.2	13.3	10.3	11.1
mod_a2	0.9	3.5	13.2	12.3	10.4	11.7

results of this procedure for two GM and two WM samples. The WC map and EP maps at 200 kHz and 1 MHz clearly show the different tissue types. The estimated values corresponding to the color scale match measured mean values of these properties in all GM and WM samples (displayed in each panel).

It is important to note that the dimensionless factor $\kappa = k_{short}/k_{long} \approx 1$ in the equation for calculating IR compensates for the signal gain fluctuations of the scanner at different TR_s. Preliminary analysis predicted that $\kappa = 0.9894$ should be used for our studies. Indeed, introducing this factor into the calculation of IR minimized the difference between measured and wEPT estimated EPs (Table 20.2). Thus, this factor

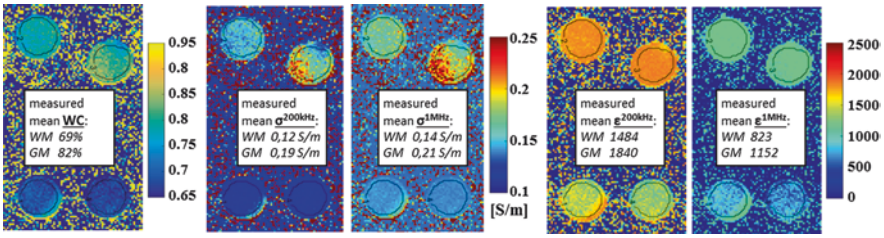

Fig. 20.3 wEPT-estimated maps of two GM (id's = {2,3} top samples) and two WM (id's = {1,4} bottom samples) excised tissue samples of calf1. Model equations used correspond to Fig. 20.4. The WC map (left), σ at 200 kHz and 1 MHz (middle), and ε_r at 200 kHz and 1 MHz (right) are presented with fixed color scales for the EPs to show their frequency dependence. In each panel, the corresponding mean values of the measurements are displayed for the two tissues. These values compare well with obtained maps

was introduced into all subsequent wEPT calculations presented in this study. Errors in wEPT estimation of IR, WC, and EPs compared to measured values were averaged among all calf tissue samples. Results are presented in Table 20.2 for wEPT estimations before κ corrections (*mod_a1*) and after (*mod_a2*). It should further be mentioned that two more adaptions have been analyzed for mapping σ at 200 kHz. When a fourth-order polynomial is used instead of the exponential form of Eq. 20.2a, $\sigma^{200\text{kHz}}$ error further reduces to 11.2%.

This first study established the feasibility of using wEPT to measure the EPs of healthy brain tissue samples. However, the study had several shortcomings:

(a) Tissue samples were measured 48–72 hours after death. Thus, we wanted to test how time from death might influence the measured EPs.
(b) Tissues samples were measured at 20–22 °C. Thus, we wanted to test how temperature might influence the measured EPs.
(c) Samples were excised prior to MRI imaging. Thus, we wanted to test if removing tissue from a bulk might influence the measured and wEPT-estimated EPs. This last point is important to clarify when establishing the use of wEPT for in vivo models.

To address these issues, a set of measurements was performed on three freshly excised calf brains (calves 4–6). Previous measurements in calves 1–3 showed that the EPs measured in different hemispheres for the same tissue type are essentially equal. Thus, the left and right hemispheres were separated to test the influence of time from death on EPs. The left hemisphere was used for measurements on the same day ("fresh" samples). The right hemisphere was preserved at 4 °C for 48 h before measurements were collected ("48 h" samples). The temperature of the brain was measured with a thermocouple to establish the effect of temperature on measurements. To account for differences in wEPT estimates that may occur when small samples are excised from the bulk, wEPT imaging was first performed on a large bulk section of cow brain. After imaging, a rectangular piece of cortex containing the thalamus was removed from the hemisphere (Fig. 20.4a) for sample

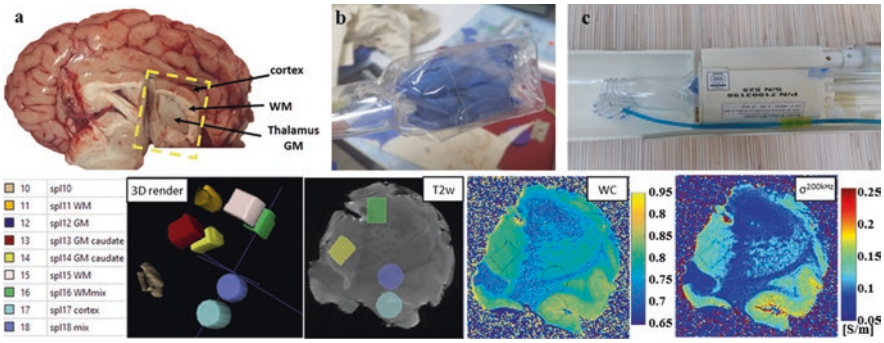

Fig. 20.4 Experimental procedures (top) and wEPT analysis (bottom) of the calf4 brain. The excised brain is separated into two hemispheres and a rectangular piece of cortex containing the thalamus is removed (**a**). Prior to sample punching, the whole brain piece is covered and wrapped for assuring tissue hydration (**b**), image taken prior to placing the sample in the coil for MR image acquisition (**c**). All samples that will be measured for their WC and EPs are segmented in the T2w image of the calf piece (bottom left). A 3D rendering of all samples is represented and one slice through samples with id's = {14, 16, 17, 18}. Corresponding T1w images with TR_s/TR_l = 700/4000 ms are loaded into MATLAB and their IR is calculated. The WC and EP maps are evaluated with the wEPT model equations; WC and σ^{200kHz} maps are displayed for the same slice in the bottom right. The outlines of the segmented tissue samples are also indicated, which can be used for evaluating mean values of estimated properties in order to be compared to their measured values

punching. To prevent dehydration, the piece was covered with a glove and a sealed-by-heat plastic bag (Fig. 20.4b) before placing it into the coil for imaging (Fig. 20.4c). Each MRI session included T1-weighted (T1w) and T2-weighted (T2w) axial scans. T1w scans were used for wEPT mapping and T2w axial scans were used for identifying brain anatomy and segmentation of excised samples (Fig. 20.4 bottom left). Details of the imaging sequences in each brain piece are as follows:

T1w axial: RARE protocol, TR = 700 ms or TR = 4000 ms, TE = 11 ms, RARE factor = 1, 4 averages, 10 slices of 1.25 mm thickness and gap of 1.25 mm between slices, FOV = 3 cm, matrix 140, in-plane resolution 214 μm, acquisition time = 6.32 min or 37.20 min. Two intercalated scans were acquired to avoid slice cross-talk artifacts.

T2w axial: RARE protocol, TR = 4400 ms, TE = 85 ms, RARE factor = 12, 12 averages, 20 slices of 1.25 mm thickness, FOV = 3 cm, matrix 140, in-plane resolution 214 μm, acquisition time = 9.40 min.

Calf brain sections were prepared for EPs and WC measurements immediately after the MRI. The orientation was marked and kept clear throughout the entire procedure. At all times, the brain sections were covered either with a glove or with a cellophane film to minimize dehydration. A minimum of nine samples per brain section was collected with 5 or 6 mm punches including 2–3 WM samples, 2 GM samples from the thalamus, and 1 additional GM sample and 2 mixed tissue

samples from the cortex. Samples were segmented from the T2w images using ITK-SNAP (Fig. 20.4 bottom left). The impedance measurements with the LCR system, the calculation of Eps, and the weighing method for WC estimation have already been described previously. At the end of the first day, two more samples were measured from the first calf (calf 4) to compare changes in the first few hours post excision. Results showed that measurements 2 h post excision are similar to those collected from samples analyzed 12 h post excision. On the following day, the EP and WC measurement procedure was repeated for the three right hemisphere brain sections.

In summary, we excised a total of 57 samples from three different calves, 30 of which were analyzed immediately after excision ("fresh") and the other 27 samples with a delay of a total of 48 h. After discarding uncertain measurements, we decided on 56 reliable WC measurements and 39 reliable EP measurements originating from calves 4–6. Results showed no significant difference between measurements in fresh calf samples compared to 48 h samples. However, certain discrepancies in comparison to the measurements of calves 1–3 can be observed (Fig. 20.5). The WC measurements were similar in calves 1–3 and calves 4–6, with a higher mean value of 73% in the WM of calves 4–6 in comparison to a mean of 69% in calves 1–3. The mean WC value in the GM remained at 82%. Higher differences have been found for EP measurements, whereas at 200 kHz calves 4–6 show lower σ values and higher ε values in both tissues, i.e., the mean $\sigma^{200\text{kHz}}$ in the WM decreased from 0.12 S/m to 0.10 S/m, in the GM from 0.19 S/m to 0.13 S/m for calves 1–3 and

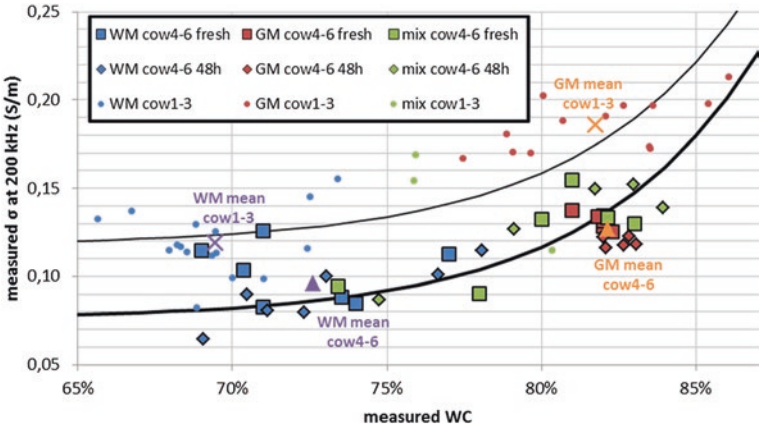

Fig. 20.5 Measurements of WC and $\sigma^{200\text{kHz}}$ in all WM (blue), GM (red), and mixed (green) samples of calves 1–3 (dots) compared to "fresh" samples of calves 4–6 (squares) and "48 h" samples of calves 4–6 (diamonds). The black lines show the best fit according to Eq. 20.2a for all calves 1–3 samples (thin line) and all calves 4–6 samples (thick line). Mean values are indicated for WM (purple) and GM (orange) for calves 1–3 samples (crosses) and calves 4–6 samples (triangle). Note the discrepancies between the first and second set of measurements in bovine brain samples, which were a result of the different storage condition before experimental procedures were established, i.e., the temperature in the refrigerator of calves 1–3 was too low

calves 4–6, respectively. For $\varepsilon^{200\text{kHz}}$, mean values are 1484 vs 1630 in the WM and 1840 vs 2487 in the GM of calves 1–3 and calves 4–6, respectively.

All calf WC and $\sigma^{200\text{kHz}}$ measurements are presented in Fig. 20.5. Colors correspond to the tissue type; marker symbols show the differences between calves 1–3 (dots) and fresh (squares) and 48 h (diamonds) samples of calves 4–6. The pairs of mean values of the WC and $\sigma^{200\text{kHz}}$ are also indicated as crosses for calves 1–3 and triangles for all calves 4–6 samples, purple markers correspond to WM samples and orange markers to GM samples. Furthermore, the lines indicate optimal fits to Eq. 20.2a for mapping σ from WC. It is obvious that the same coefficients used in Eq. 20.2a for the calves 1–3 measurements (thin black line) will not best represent the new measurements from calves 4–6 (thick black line).

Furthermore, a slightly different combination of TR_s was used in the two T1w images of the wEPT imaging sequence for calves 4–6, i.e., TR_s = 700 ms and TR_l = 4000 ms were used instead of TR_l being 3000 ms as was the case for calves 1–3 studies. Therefore, the coefficients in Eq. 20.1 had to be refitted for altered values of IR. This model will be designated as *mod_b*, with coefficients $w_1 = 1.3028$ and $w_2 = 0.9134$. In a next step, two new sets of coefficients for Eq. 20.2a were created from the measurements of calves 4–6, one for mapping from WC to $\sigma^{200\text{kHz}}$ (thick black line in Fig. 20.5) and one for $\sigma^{1\text{MHz}}$. The new coefficients were found via curve fitting, c_1 = 0.0759, c_2 = 1.2351E-08, and c_3 = 18.7575 for 200 kHz and c_1 = 0.0952, c_2 = 2.1919e-08, and c_3 = 18.1696 for 1 MHz. This model is called *mod_c*.

Typical wEPT model analysis, including WC and σ map creation, is illustrated in Fig. 20.4 at the bottom right. The presented slice corresponds to the T2w image that was used for segmentation. Therefore, it is possible to use the segmentation data and calculate mean values of WC and σ in a 3D representation of each tissue sample. The mean values can be compared to the corresponding measurement as presented in Table 20.3 for both tested models. Although an average error for WC estimation of 2.5% with *mod_b* is very low, the errors in the σ estimates are high. As expected, Eq. 20.2a derived from the data for calves 1–3 (*mod_b*, thin line in Fig. 20.5) does not optimally fit the measured WC and σ values of calves 4–6. The adequate wEPT model *mod_c* performs well for σ estimates with average errors as low as 13.6% for 200 kHz and 13.3% for 1 MHz.

We also conducted experiments to estimate the temperature dependence of the properties. Another calf brain was measured 24 hour post excision for this experiment. Four samples were extracted for these tests: two GM samples from the thalamus and two WM samples. Each sample was 5 mm thick and 5 mm in diameter. The base temperature of the samples was 20 °C. Samples were placed in the plate to be

Table 20.3 Average relative error of wEPT estimates in all brain samples of calves 4–6 compared to measured values

	WC (%)	$\sigma^{200\text{kHz}}$ (%)	$\sigma^{1\text{MHz}}$ (%)
mod_b	2.5	41.1	30.7
mod_c	3.3	13.6	13.3

measured with the Ag/AgCl electrodes. In order to gradually warm the tissue samples in the plate, lab gloves filled with hot water (~70 °C) were positioned around the setup and fixated to keep it heated. A thermocouple was placed on the plate next to the electrode to monitor the temperature. When the temperature increased sufficiently, the electrodes were removed and the thermocouple was inserted into the sample to measure the actual tissue temperature. When the temperature increased a few degrees, LCR measurements of the impedance were manually logged in the notebook at a single frequency of 200 kHz.

Measurements of $\sigma^{200\text{kHz}}$ for increasing sample temperature are shown in Fig. 20.6. The exponential trend lines for GM (blue) and WM (red) are displayed. Two conclusions can be drawn from this study. When the body temperature of 37 °C is assumed, this would result in GM conductivity of 0.194 S/m and for the WM 0.102 S/m, which are in good agreement with values reported in the literature, e.g., $\sigma^{\text{GM}} = 0.25$ S/m and $\sigma^{\text{GM}} = 0.12$ S/m at 200 kHz were assumed in previous simulation studies [47]. Second, our measurements of excised samples were conducted at a room temperature of about 21 °C. According to these results, the multiplication factor for increasing σ from 21 °C to 37 °C is very similar. Note that this will be important when conducting in vivo wEPT studies because the temperature of tissues imaged in live animals are higher than in excised samples.

20.2.4 In Vivo wEPT Study: Healthy and Tumor-Bearing Rats

One of the main objectives of this study was to investigate if the wEPT approach can be used to create in vivo maps of WC and σ in rat brain tumor models. In order to establish optimal experimental procedures and validate the wEPT model, a study was performed in one healthy rat (Fisher F334 rat, male, 10.2 weeks old from Envigo, USA). Similar to the bovine brain experiments, 16 tissue samples were taken from the excised brain and T1, WC, and EPs were measured. But prior to euthanizing the animal (Pentane 1 ml injected into the thorax cage after strong

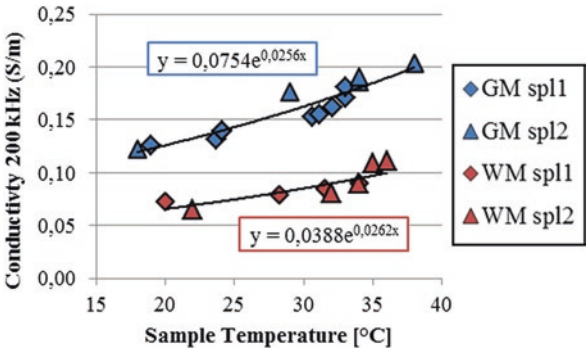

Fig. 20.6 Temperature-dependence of conductivity at 200 kHz for sample temperatures between ~18 and 38 °C. σ was measured for two GM (blue) and two WM (red) samples of one calf brain. Exponential trend lines are displayed for both tissues

anesthetization with ketamine/xylasine), we performed in vivo MRI imaging of the rat with the inclusion of the wEPT sequence (two T1w images with different TR_s).

In more detail, the live animal was anesthetized with isoflurane (2%) and placed in the rat head coil of the MRI in the prone position. The brain was first localized in the axial, sagittal, and coronal position. Twelve slices were chosen orthogonally to the brain covering the olfactory bulb (front part of brain) to the cerebellum (back of the brain) (Fig. 20.7 top). A T2w image and corresponding stacks of T1w images for T1 value estimation and wEPT analysis were acquired. General image sequence parameters remain the same as previously listed (compare Sect. 20.2.3) The whole brain was excised and placed in a rat brain slicer (Zivic labs) to subsequently extract cylindrical samples (Fig. 20.7 middle). Two blades with a measured thickness of 0.2–0.3 mm were inserted in the slicer. We used a 3.5 mm punch and obtained three samples from the front of the brain, six samples from the midbrain (Fig. 20.7 middle), three samples from the hindbrain, and four more samples of the remainder of the back brain, which were not imaged in vivo because it was outside the FOV.

After sample preparation, impedance measurements were taken with the LCR meter and their EPs estimated using the known sample dimensions. The T1 value of the samples was evaluated with MR imaging using the variable TR method, which includes images for further wEPT analysis (T1w images with TR_s/TR_l = 700/4000 ms). In order to monitor tissue dehydration in the MRI, the samples have been weighed pre- and post imaging. The sample WC was again estimated as the difference between wet and dry weights.

Experimental results predicted lower WC values in the rat samples than expected, which could be a result of the very small sample size possibly leading to fast drying of tissue. Furthermore, tissue samples of the rat are far more heterogeneous than in the calf. Thus, σ measurements of rat samples only showed a very minor increase in average values of GM compared to the WM samples. In conclusion, it is not recommended to use the 16 measurements of the rat samples to create a new wEPT model (finding coefficients that best match Eqs. 20.1 and 20.2a). Instead, we employed the wEPT models originating from calf measurements.

The ex vivo MRIs were analyzed in the same manner as calves 1–3 and calves 4–6, i.e., the two T1w images were loaded, maps were created, and mean values of estimated properties were calculated according to the segmentation masks of each sample. We used the previously described *mod_b* and *mod_1* settings for wEPT analysis. Table 20.4 summarizes average errors of wEPT estimates of WC, σ^{200kHz}, σ^{1MHz} compared to measurements in all 16 rat1 samples. Higher deviations of measured values were observed for the rat versus calf data. The higher WC errors might be related to the measurement problems of WC encountered in the small rat samples.

Surprisingly, the model that performed the best for σ estimation with wEPT was *mod_b* (calves 1–3 data) with the lowest average relative errors for both frequencies, 200 kHz and 1 MHz. However, the worst case of average error is 23.9% for σ estimations at 200 kHz, which is still reasonable given the high heterogeneity in the

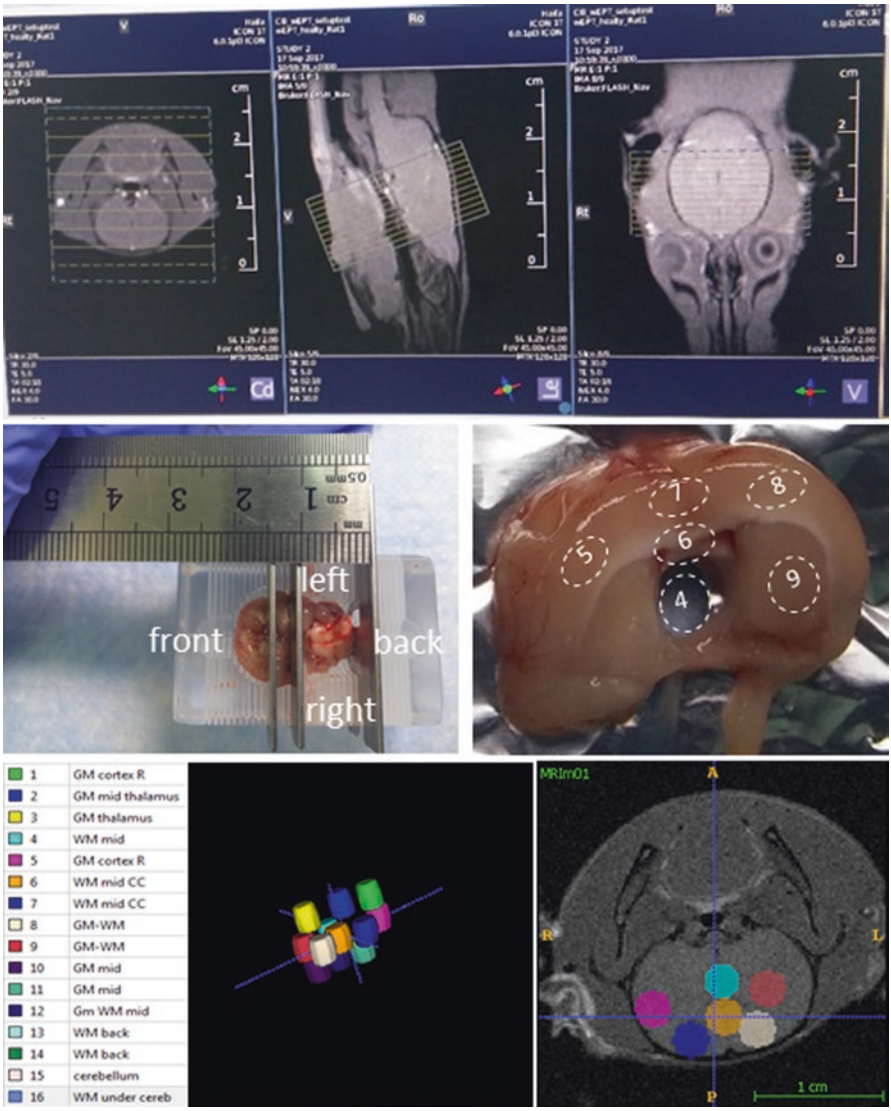

Fig. 20.7 Experimental procedures in healthy rat1. (top) The in vivo MRI localization of the brain in axial, coronal, and sagittal views. (middle) Excised brain in the brain slicer and slice of mid-brain, where one sample with id = 4 is already punched out. The locations of five additionally planned punch sites are indicated. (bottom) Corresponding sample segmentation in ITK-Snap along with a 3D rendering of 12 tissue samples with their labels and one corresponding slice through samples with the same id = {4–9}

Table 20.4 Average error of wEPT estimates in all brain samples of rat1 compared to measured values

	WC (%)	σ^{200kHz} (%)	σ^{1MHz} (%)
mod_b	7.4	21.7	19.1
mod_c	6.6	23.9	20.2

samples as compared to calf experiments. Also note that given the small sample size, many pixels in the MRI image corresponded to more than one tissue sample which might also affect the results. In general, reported mean values of wEPT estimations depend on the quality of the segmentation.

Subsequently, the in vivo MRI data of healthy rat1 was analyzed. This was the first time an imaging dataset of a live animal was used with a more realistic 3D representation of the excised samples (Fig. 20.7 bottom). However, recall that only 12 of the 16 samples were visible in the in vivo wEPT studies. The wEPT sequence consisted of two T1w images (TR_s/TR_l = 700/4000 ms) each with 12 slices through the rat's brain (Fig. 20.7). wEPT analysis again yielded maps of IR, WC, σ^{200kHz}, and σ^{1MHz}, which were created with MATLAB (data not shown, but compare Fig. 20.9 of a tumor-bearing rat) and the corresponding segmentation consisting of 3D masks for each tissue sample can be used to evaluate mean values of the estimations.

In addition to *mod_b* and *mod_c*, another wEPT model termed *mod_d* was created that used that accounts for the temperature dependency of T1 and σ based on the calves 4–6 dataset (Fig. 20.6). The T_1 relaxation value of tissue is not only dependent on the imaging frequency but also on the temperature. In order to account for these changes, the estimated T1 values in the ex vivo samples of rat1 at 20–22 °C were compared to the corresponding T1 values in the in vivo images at 35–37 °C. Results predicted a multiplication factor of 1.3003 of T1 values for increasing the temperature. Since the WC of tissue is independent of temperature, it follows that the calculated IR has to be multiplied by a factor of $IR^{TempCor}$ = 0.8587 to obtain adapted IR values that are valid for in vivo MRI data. The T1 plateau for the high CSF value at 37 °C could not be reached; therefore, no reliable results could be obtained for the CSF with our scanner. Thus, for temperature adjustment of the CSF values, the same factor of 0.8587 was used to reduce the IR. After correcting IR values, curve fitting was applied to find the new coefficients of Eq. 20.1 in *mod_d*, which were found to be w_1 = 1.2598 and w_2 = 1.0384. Subsequently, the conductivity values of all brain tissue samples of calves 4–6 were multiplied by a factor of $\sigma^{TempCor}$ = 1.49 (at 200 kHz and 1 MHz) to account for increased conductivity at an in vivo temperature of 37 °C. A previous experiment (Fig. 20.6) revealed that the increase of σ with temperature is only slightly different for GM and WM; therefore, the average of the two evaluated factors was chosen for $\sigma^{TempCor}$. The same factor was used for conductivity adjustments of all brain samples at 1 MHz, although the preliminary study was only performed for 200 kHz. The conductivity of CSF was assumed to be 1.67 S/m at both frequencies. For the completion of *mod_d*, curve fitting was applied to find the coefficients in Eq. 20.2a, c_1 = 0.1214,

c_2 = 2.4469e-8, c_3 = 18.2031 for 200 kHz and c_1 = 0.1481, c_2 = 6.9562e-8, c_3 = 17.1286 for 1 MHz.

It should be mentioned that curve fitting was also repeated for σ mapping for adjusting sample values with a tissue-type specific factor (one for GM, one for WM). The results for the coefficients c_1,c_2,c_3 were the same for 200 kHz and only slightly different at 1 MHz. Therefore, any other temperature-dependent adaptations of the conductivity were neglected.

Average values for WC, $\sigma^{200\text{kHz}}$, and $\sigma^{1\text{MHz}}$ estimations of the three wEPT models (*mod_b*, *mod_c*, *mod_d*) were evaluated in the 12 tissue samples visible in the in vivo study. The average error to corresponding measurements are presented in Table 20.5. For comparing measured σ values to wEPT estimates with *mod_d*, the recorded mean values in the samples which correspond to in vivo temperature have to be adjusted by multiplying with 0.67 (the reciprocal of σ^{TempCor}). As was the case for the ex vivo studies, errors of WC estimates are relatively high, which might be due to already mentioned measurement errors. Surprisingly, conductivity estimations were best for *mod_b* and higher average errors were found for *mod_c*, as expected. Model *mod_d*, which was specifically derived for in vivo studies, shows average errors for the σ estimations of 18.6% and 16.8% for 200 kHz and 1 MHz, respectively.

It should be noted that the difference in average errors in the in vivo wEPT model might appear lower compared to the ex vivo errors (Table 20.4) because the segmentation of the in vivo images represents a larger portion of the actual tissue sample. The brain samples of the rat brain are far more heterogeneous than those of the calf, making it difficult to estimate EP values from the impedance measurements. Furthermore, the small brain samples are only partially visible in the ex vivo MRIs, which may explain the variation in reported values. Therefore, to improve the measurement and imaging data for the tumor-bearing rats, the protocol was adjusted such that larger (but fewer) tissue samples were collected.

Four tumor-bearing F334 rats (rats 2–5) have been investigated during this study. The main goals were to create in vivo maps of WC and σ and to obtain measurements of excised tumor samples and compare them to measurements of their contralateral counterparts. Two tumor types, RG2 cells in rat2 and F98 cells in rats 3–5, were considered.

Under general anesthesia (isoflurane for induction and then i.p. injection of xylasine 10 mg/kg/ketamine 75 mg/kg), the rat head was shaved and the animal immobilized on the stereotactic unit. After disinfection and incision of the skin of the

Table 20.5 Average error of *in vivo* wEPT estimates from the 12 imaged brain samples of rat1 compared to measured values

	WC (%)	$\sigma^{200\text{kHz}}$ (%)	$\sigma^{1\text{MHz}}$ (%)
mod_b	5.2	12.5	11.1
mod_c	7.2	41.8	32.9
mod_d	5.5	18.6	16.8

head, a hole was drilled through the skull at coordinates corresponding to the right thalamus (2.5 mm lateral to midline, 1 mm anterior to the coronal fissure). A 10 µl mixture of cells (5000 cells in rats 2–3 and 10,000 cells in rats 4–5) and matrigel matrix ref. 354,263 (1:1) was slowly injected with a 0.5 cc insulin syringe 30 G, at a depth of 3 mm under the dura. The syringe was placed vertically. The muscles and skin were sutured 2 minutes after the injection. The analgesic Calmogine (Vitoquenol) was injected subcutaneously 10 mg, and another analgesic (Buprenorphine, 2 mg/ml) was delivered via the drinking water throughout the experiment.

MRI images were acquired at selected time points: rat2 was imaged 7, 13, an 15 days after cell injection; rat3 at 7,13, 16, and 19 days after injection; and rats 4–5 at 10 and 14 days. Before each imaging session, rats were anesthetized using 2% isoflurane in air (SomnoSuite, Kent Instruments) and placed in the prone position into the dedicated head coil. The MRI sequence protocol was identical to that of healthy rat1. However, the T2w axial scan now also contributes to tumor detection and to the brain slicing and sampling plans as well as the segmentation of the ex vivo samples and tumor. Figure 20.8 plots the estimated tumor volume in the four tumor-bearing rats according to the T2w MRIs that have been acquired at different days after tumor cell injection.

After the final in vivo MRI, each rat was sacrificed by overdose of pentobarbital and the whole brain was carefully removed in one piece as depicted in the top left of Fig. 20.9. The excised brain was placed in the brain slicer and three slices per animal were created. Samples were punched out using 5 mm punches whenever possible. One tumor sample and the corresponding contralateral sample were taken from the middle slice, as shown at the top of Fig. 20.9. The brain, the slices, and the tissue samples were covered with a glove or cellophane film when-

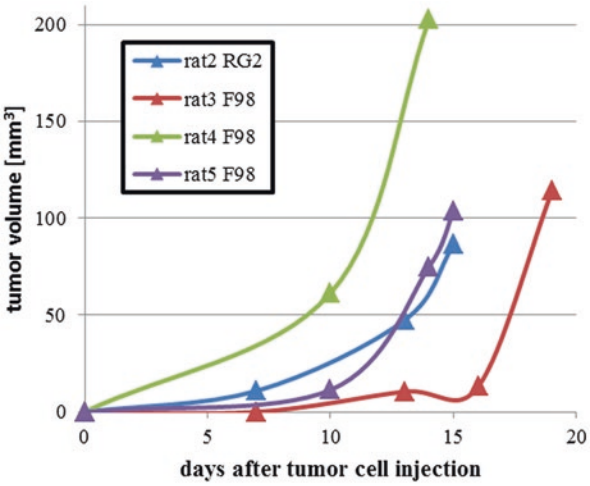

Fig. 20.8 Tumor volume estimated by T2w imaging segmentation over time for four tumor-bearing rats

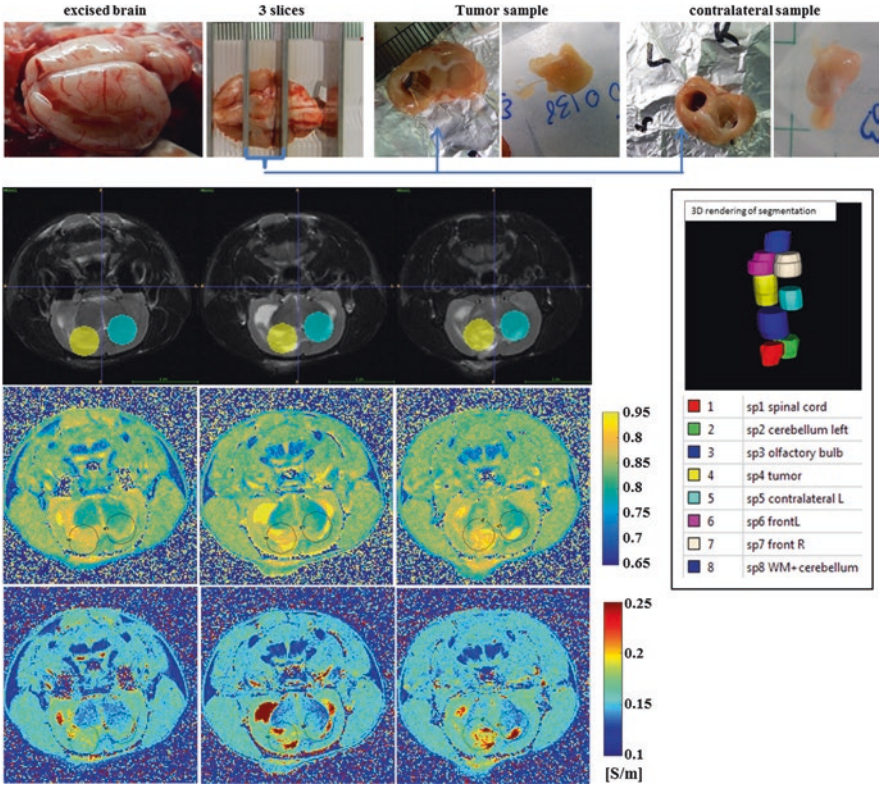

Fig. 20.9 Experimental procedures in F98 tumor-bearing rat5 for the final in vivo MRI images, which were acquired 14 days post-injection of tumor cells. (top) The excised brain was cut into three slices, the middle one containing the tumor and contralateral samples. The three slices corresponding to the middle brain slice containing the tumor (id = 4, yellow) and contralateral sample (id = 5, cyan). These three slices are reproduced in the T2w image with the overlaid segmentation (middle). A 3D rendering with the label description is provided to the right. (bottom) Corresponding WC and $\sigma^{200\text{kHz}}$ maps are presented. Outlines of the segmentation are superimposed on these maps

ever possible during the experimental procedures to minimize dehydration. WC and EP measurements were obtained using the previously described LCR meter and the weighing method. Different numbers of samples were punched out from the four rat brains, the middle slice contains the tumor sample and the contralateral sample (Fig. 20.9). We did not measure EPs in all of the samples. However, we had combined measurements of WC and EPs in six samples of rats 2–4 and five samples of rat5 (id's = {4-8}), including tumor and contralateral samples in all animals.

It was expected that the tumor sample would have the highest WC and consequently also the highest σ values. This was almost always the case, except in rat2, where one sample from the right part of the front of the brain had an unrealistically high value of 94%. The measured WC values of the samples for each rat are shown

in the top plot of Fig. 20.10. The red crosses indicate the tumor sample, which indeed have the highest measured WC in rats 3–5. The contralateral sample is indicated by a yellow cross. Also note, that rat2 not only had one very high measurement of a brain tissue sample but also the measured tumor WC is lower than the WC of the contralateral sample.

According to the σ measurements at 200 kHz (Fig. 20.10 bottom), the tumor only has the highest conductivity in rat3 and rat5, it is however always higher than the conductivity of the contralateral sample. This increase is even more pronounced for σ measurements at 1 MHz (data not shown).

Subsequently, we performed wEPT analysis with the final in vivo MRI data from the four tumor-bearing rats. As an example, WC and $\sigma^{200\text{kHz}}$ maps are reproduced for rat5 in the bottom part of Fig. 20.9. The tumor and contralateral samples were visible in three slices of the MRI dataset. Anatomical structures are well represented in both maps. The higher WC fraction and the higher conductivity in the tumor compared to the contralateral sample are clearly visible. The mean values of wEPT estimations of WC and σ were calculated according to the sample segmentation. Similar to the studies in healthy rat1, we considered *mod_b*, *mod_c*, and *mod_d*. Average errors obtained in all 23 samples from rats 2–5, including the tumor sample are presented in Table 20.6. A particularly low average error of WC estimations of 2.2% are predicted for *mod_b* and *mod_d*. Generally, the average errors for WC estimation are lower in the tumor-bearing rats than in healthy rat1, which might again indicate measurement errors in the WC of rat1. For wEPT esti-

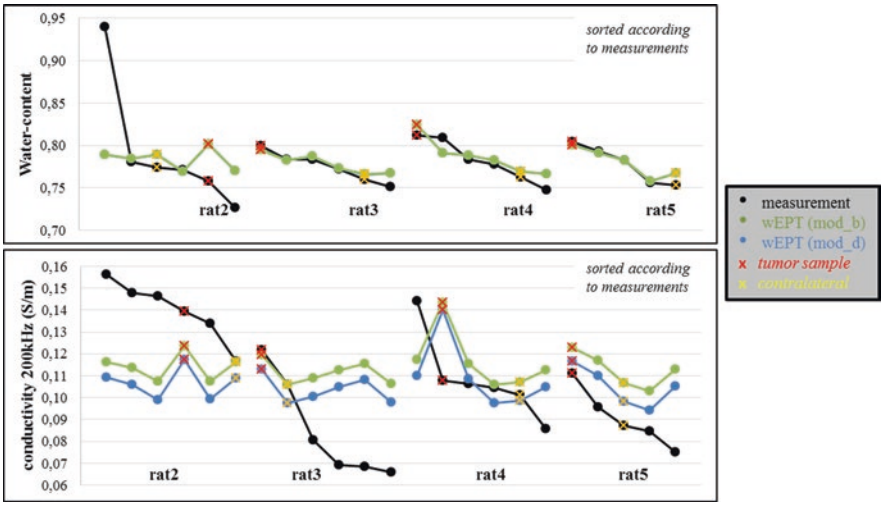

Fig. 20.10 Measured and wEPT-estimated values of WC (top) and $\sigma^{200\text{kHz}}$ (bottom) in six samples of rats 2–4 and five samples of rat5. The data is sorted according to the measurements (black). The mean values in the corresponding sample according to wEPT estimations are displayed, *mod_b* (green), *mod_d* (blue). Tumor samples are indicated with a red cross and contralateral samples in yellow

Table 20.6 Average error of *in vivo* wEPT estimates compared to measured values in all tissue samples (including the tumor sample) of rats 2–5

	WC (%)	$\sigma^{200\text{kHz}}$ (%)	$\sigma^{1\text{MHz}}$ (%)
mod_b	2.2	22.1	20.9
mod_c	6.7	110.2	80.2
mod_d	2.2	23.3	21.6

mations of σ, the best performing model is surprisingly *mod_b*. However, the average error for $\sigma^{200\text{kHz}}$ in wEPT estimations with the in vivo model *mod_d* is only slightly higher with 23.3%. And as expected, *mod_c* does not produce accurate estimations of WC or σ.

The wEPT estimations of WC and $\sigma^{200\text{kHz}}$ of the two best performing models are also displayed in Fig. 20.10 for each samples, *mod_b* in green and *mod_d* in blue. The top part of Fig. 20.10 indicates that WC estimations with the wEPT approach matches the measurements quite well. It is also likely that the wEPT estimations in rat2 are more realistic than the actual measurements, given the high outlier and also the low tumor WC. The trend for σ estimations is not the same when compared to the measurements in the rat samples (Fig. 20.10 bottom). When σ is estimated with the wEPT approach, the tumor always has the highest value, i.e., the sample with the red cross has the highest conductivity. Thus, the contralateral sample always shows lower conductivity than the tumor in each animal for measurements and wEPT-estimated values contrary to the measurements.

20.3 Summary and Discussion

In this study, we investigated if the wEPT approach can be adapted for mapping EPs, specifically the conductivity of brain tissue, between 200 kHz and 1 MHz. We conducted experimental measurements and wEPT analysis in a phantom study with BSA solutions, in tissue samples excised from calf and rat brains, and in tumor-bearing rat models. The wEPT analysis included model creation and estimation analysis, i.e., first the optimal coefficients of mapping functions for WC and EP have to be found, then the maps can be created and values in different areas can be estimated and compared to corresponding measurements.

The feasibility study with four BSA solutions of varying albumin concentrations predicted good agreement between experimentally measured values of IR, WC, σ, and ε at 200 kHz and 1 MHz and wEPT estimations (Table 20.1). We then performed extensive studies with excised calf brain samples. We measured properties (T1, WC, and EP between 20 Hz and 1 MHz) of excised samples of WM and GM (Fig. 20.1). New wEPT models have been developed based on this data (Figs. 20.2 and 20.5), i.e., optimal coefficients in mapping functions (IR➔ WC, WC➔ σ, WC➔ ε) have been estimated by curve fitting. Maps of WC and EPs at 200 kHz and 1 MHz

have been created for excised calf samples and pieces of calf brain with the wEPT imaging approach (Fig. 20.3 and Fig. 20.4). Tissue types can be distinguished in the maps and average errors compared to measurements are low for WC (<3.5%) and reasonable for σ estimations at 200 kHz (<13.6%), compare Tables 20.2 and 20.3.

The next set of studies was performed in rat models, using one healthy rat and four tumor-bearing rats. Experimental measurements revealed WC and EPs of brain tissue samples and tumor samples excised postmortem (Figs. 20.7 and 20.9). Previously derived wEPT model equations were used to study in vivo images of the rats. Furthermore, we created an adapted wEPT model that incorporates adjustments considering the temperature dependence of T1 values and σ of brain tissue (Fig. 20.6). WC and $\sigma^{200\text{kHz}}$ maps were created for the animals and analyzed (Fig. 20.9). The brain anatomy, distribution of different tissue types, and also the tumor are clearly visible in the created maps. Average errors between measurements and wEPT estimations were calculated (Tables 20.5 and 20.6). WC estimations show low average errors and correspond very well to the measurements in each sample (Fig. 20.10). Average errors of $\sigma^{200\text{kHz}}$ estimations in all samples including the tumor samples were reasonable (22–23%). Yet, wEPT estimations predict highest WC and σ in the tumor sample, which although expected was not that case for our measurements in all animals. For example rat2 and rat4 measurements predict higher σ values in healthy brain tissue.

However, at this point it should be noted that we estimated measurement errors for WC of ±1% and measurement errors of σ of ±10%. Measurement quality is dependent on tissue sample preparation and handling. For example, the differences between measurements of calves 1–3 and calves 4–6 may come from different storage conditions in the office vs. in the butcher refrigerator. Too cold temperature in the butcher refrigerator could generate the higher conductivity we observed in calves 1–3. Furthermore, we saw some discrepancies in the WC measurements of healthy rat1, possibly because of fast drying of samples of small sample size. Furthermore, the samples of rat brain are more heterogeneous and it is difficult to obtain samples that only represent one type of tissue. Figure 20.11 summarizes the measurements of WC and $\sigma^{200\text{kHz}}$ in all tissue samples.

In the first studies, we also concentrated on estimations of the relative permittivity ε_r, which were neglected in later investigations. This is due to the fact that we are most interested in applying the wEPT approach for modeling induced electric fields during Optune treatment of patients with GBM. Computational studies have shown that at a frequency of 200 kHz, the field is almost completely shaped by the tissue conductivity [25]. Furthermore, relative errors from calves 1–3 data revealed better agreement than the conductivity mapping results. This is somewhat surprising given the fact that the permittivity is not strictly increasing for increasing water content of the tissue at our frequency range because the CSF with the highest water content has the lowest permittivity.

However, on a general note, all reported wEPT-estimated mean values are dependent on the underlying sample segmentation. For higher image resolution, a bigger section of the samples can be imaged and used for the estimations. For ex vivo wEPT studies, we usually had only one MRI slice through the sample with a lower

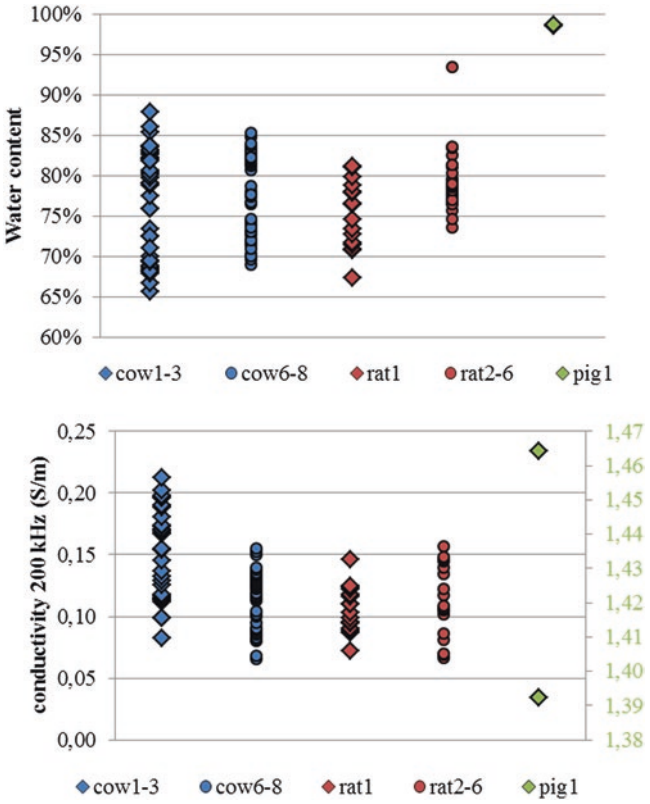

Fig. 20.11 Measurements of WC (top) and $\sigma^{200\text{kHz}}$ (bottom) all tissue samples originating from different animal samples

number of pixels contributing to the tissue, compared to in vivo wEPT studies with a more realistic 3D representation of samples. Yet, additional experiments might be necessary for validation of the adapted in vivo wEPT model. Specifically, the temperature dependence of EPs of brain tissue might be investigated in more detail.

Also, wEPT is an imaging technique for estimating WC and EPs. Thus, the results are dependent on imaging quality and general procedures for reprocessing (such as denoising algorithms) might be studied in more detail. The authors of the original wEPT article further investigated the effect of B_1 inhomogeneities and found that errors may reach ±20% for σ and ± 11% for ε_r estimations. Yet their approach was described for a frequency of 128 MHz and it was conducted with a 3 T MRI scanner.

In conclusion, with our adapted wEPT approach, the frequency independent WC maps produce reliable results. It remains questionable if the relationship between WC and EPs of healthy and pathological tissues for frequencies in the 100–1000 kHz range is sufficient. At frequencies lower than 10 kHz, cell membranes act as capaci-

tive elements because of their low conductivity. As the frequency increases, this membrane capacitance effect disappears, allowing electric currents to flow more freely according to the local ionic conductivity. As a result, the EPs of the tissues become highly correlated with the tissue water fraction. According to our results, adapting wEPT to frequencies between 100 and 1000 kHz is likely at the verge of producing reliable results. In future studies, the approach might be enhanced by including adaptations according to additional radiological features derived from other imaging modalities, such as T2-weighted imaging or diffusion imaging.

Improving and refining an approach for non-inversely mapping the EPs within the brain would be of high interest for planning and adapting the Optune treatment. Some studies have already been conducted with optimized EPT sequences for reconstructing EPs in brain tumors [48–50]. Results predict higher conductivity in the tumor compared to healthy tissue and a greater variability of EPs in individual tumor areas among patients. However, the wEPT approach would be of particular interest because it only requires two T1w images, which resemble the conventional T1 and proton density (PD) images that are acquired routinely. A preliminary study has already been conducted and WC and σ maps have been created for three GBM patients. Results will be presented in a future publication.

References

1. Miklavčič, D., Pavšelj, N., & Hart, F. X. (2006). Electric properties of tissues. In M. Akay (Ed.), *Wiley encyclopedia of biomedical engineering*. https://doi.org/10.1002/9780471740360.ebs0403.
2. Collins, C. M., & Wang, Z. (2011). Calculation of radiofrequency electromagnetic fields and their effects in MRI of human subjects. *Magnetic Resonance in Medicine, 65*(5), 1470–1482.
3. Voigt, T., Homann, H., Katscher, U., & Doessel, O. (2012). Patient-individual local SAR determination: In vivo measurements and numerical validation. *Magnetic Resonance in Medicine, 68*(4), 1117–1126.
4. Zhang, X., Schmitter, S., Van de Moortel, P.-F., Liu, J., & He, B. (2013). From complex B1 mapping to local SAP estimation for human brain MR imaging using multi-channel transceiver coil at 7T. *IEEE Transactions on Medical Imaging, 32*(6), 1058–1067.
5. Restivo, M. C., et al. (2015). Local specific absorption rate in brain tumors at 7 tesla. *Magnetic Resonance in Medicine, 00*, n/a-n/a.
6. Makarov, S., et al. (2017). Virtual human models for electromagnetic studies and their applications. *IEEE Reviews in Biomedical Engineering, 10*, 95–121.
7. Barker, A. T., Jalinous, R., & Freeston, I. L. (1985). Non-invasive magnetic stimulation of human motor cortex. *Lancet, 1*, 1106–1107.
8. Nitsche, M. A., & Paulus, W. (2001). Sustained excitability elevations induced by transcranial DC motor cortex stimulations in humans. *Neurology, 57*, 1899–1901.
9. Miranda, P. C., Salvador, R., Wenger, C., & Fernandes, S. R. (2016). Computational models of non-invasive brain and spinal cord stimulation. In *Engineering in medicine and biology society (EMBC), 2016 38th annual international conference of the IEEE*.
10. Joines, W. T., Zhang, Y., & Jirtle, R. L. (1994). The measured electrical properties of normal and malignant human tissues from 50 to 900 MHz. *Medical Physics, 21*(4), 547–550.

11. Haemmerich, D., Staelin, S. T., Tsai, J. Z., Tungjitkusolmun, S., Mahvi, D. M., & Webster, J. G. (2003). In vivo electrical conductivity of hepatic tumours. *Physiological Measurement, 24*(2), 251–260.
12. Haemmerich, D., Schutt, D. J., Wright, A. W., Webster, J. G., & David, M. (2009). Electric conductivity measurements of excised human metastatic liver tumours before and after thermal ablation. *Physiological Measurement, 30*(5), 459–466.
13. Surowiec, A. J., Stuchly, S. S., Barr, J. R., & Swarup, A. (1988). Dielectric properties of breast carcinoma and the surrounding tissues. *IEEE Transactions on Biomedical Engineering, 35*(4), 257–263.
14. Lu, Y., Li, B., Xu, J., & Yu, J. (1992). Dielectric properties of human glioma and surrounding tissue. *International Journal of Hyperthermia, 8*(6), 755–760.
15. Foster, K. R., & Schwan, H. P. (1989). Dielectric properties of tissues and biological materials: A critical review. *Critical Reviews in Biomedical Engineering, 17*(1), 25–104.
16. Laufer, S., Ivorra, A., Reuter, V. E., Rubinsky, B., & Solomon, S. B. (2010). Electrical impedance characterization of normal and cancerous human hepatic tissue. *Physiological Measurement, 31*(7), 995–1009.
17. Ivorra, A., Al-Sakere, B., Rubinsky, B., & Mir, L. M. (2009). In vivo electrical conductivity measurements during and after tumor electroporation: Conductivity changes reflect the treatment outcome. *Physics in Medicine and Biology, 54*(19), 5949–5963.
18. Kirson, E. D., et al. (2004). Disruption of cancer cell replication by alternating electric fields. *Cancer Research, 64*(9), 3288–3295.
19. Kirson, E. D., et al. (2007). Alternating electric fields arrest cell proliferation in animal tumor models and human brain tumors. *Proceedings of the National Academy of Sciences of the United States of America, 104*(24), 10152–10157.
20. Stupp, R., et al. (2012). NovoTTF-100A versus physician's choice chemotherapy in recurrent glioblastoma: A randomised phase III trial of a novel treatment modality. *European Journal of Cancer, 48*(14), 2192–2202.
21. Stupp, R., et al. (2015). Maintenance therapy with tumor-treating fields plus temozolomide vs temozolomide alone for glioblastoma. A randomized clinical trial. *JAMA, 314*(23), 2535–2543.
22. Fonkem, E., & Wong, E. T. (2012). NovoTTF-100A: A new treatment modality for recurrent glioblastoma. *Expert Review of Neurotherapeutics, 12*, 895–899.
23. Mrugala, M. M., et al. (2014). Clinical practice experience with NovoTTF-100A™ system for glioblastoma: The patient registry dataset (PRiDe). *Seminars in Oncology, 41 Suppl 6*(5), S4–S13.
24. Chaudhry, A., et al. (2015). NovoTTF™-100A system (tumor treating fields) transducer array layout planning for glioblastoma: A NovoTAL™ system user study. *World Journal of Surgical Oncology, 13*, 316.
25. Miranda, P. C., Mekonnen, A., Salvador, R., & Basser, P. J. (2014). Predicting the electric field distribution in the brain for the treatment of glioblastoma. *Physics in Medicine and Biology, 59*(15), 4137–4147.
26. Wenger, C., Salvador, R., Basser, P. J., & Miranda, P. C. (2015). The electric field distribution in the brain during TTFields therapy and its dependence on tissue dielectric properties and anatomy: A computational study. *Physics in Medicine and Biology, 60*(18), 7339.
27. Wenger, C., Salvador, R., Basser, P. J., & Miranda, P. C. (2016). Improving tumor treating fields treatment efficacy in patients with glioblastoma using personalized array layouts. *International Journal of Radiation Oncology, Biology, Physics, 94*(5), 1137.
28. Korshoej, A. R., Hansen, F. L., Thielscher, A., Von Oettingen, G. B., Christian, J., & Hedemann, S. (2017). Impact of tumor position, conductivity distribution and tissue homogeneity on the distribution of tumor treating fields in a human brain: A computer modeling study. *PLoS One, 12*(6), e0179214.
29. Lok, E., San, P., Hua, V., Phung, M., & Wong, E. T. (2017). Analysis of physical characteristics of tumor treating fields for human glioblastoma. *Cancer Medicine, 6*(6), 1286–1300.

30. Gabriel, C., Gabriel, S., & Corthout, E. (1996). The dielectric properties of biological tissues: I. Literature survey. *Physics in Medicine and Biology, 41*(11), 2231–2249.
31. Gabriel, C., Peyman, A., & Grant, E. H. (2009). Electrical conductivity of tissue at frequencies below 1 MHz. *Physics in Medicine and Biology, 54*(16), 4863–4878.
32. Lu, Y., Li, B., Xu, J., & Yu, J. (1992). Dielectric properties of human glioma and surrounding. *International Journal of Hyperthermia, 8*(6), 755–760.
33. Wenger, C., et al. (2018). A review on tumor treating fields (TTFields): Clinical implications inferred from computational modeling. *IEEE Reviews in Biomedical Engineering, 11*, 195–207.
34. Metherall, P., Barber, D. C., Smallwood, R. H., & Brown, B. H. (1996). Three-dimensional electrical impedance tomography. *Nature, 380*(6574), 509–512.
35. Griffiths, H., Stewart, W. R., & Gough, W. (1999). Magnetic induction tomography. A measuring system for biological tissues. *Annals of the New York Academy of Sciences, 873*, 335–345.
36. Woo, E. J., & Seo, J. K. (2008). Magnetic resonance electrical impedance tomography (MREIT) for high-resolution conductivity imaging. *Physiological Measurement, 29*, R1–R26.
37. Joy, M. L., Scott, G. C., & Henkelman, R. M. (1989). In vivo detection of applied electric currents by magnetic resonance imaging. *Magnetic Resonance Imaging, 7*(1), 89–94.
38. Katscher, U., Kim, D.-H., & Seo, J. K. (2013). Recent progress and future challenges in MR electric properties tomography. *Computational and Mathematical Methods in Medicine, 2013*, 546562.
39. Haacke, E. M., Brown, R. W., Thompson, M. R., & Venkatesan, R. (1999). *Magnetic resonance imaging physical principles and sequence design*. New York: Wiley.
40. Zhang, X., Liu, J., & He, B. (2014). Magnetic resonance based electrical properties tomography: A review. *IEEE Reviews in Biomedical Engineering, 7*, 87–96.
41. Michel, E., Hernandez, D., & Lee, S. Y. (2017). Electrical conductivity and permittivity maps of brain tissues derived from water content based on T 1 -weighted acquisition. *Magnetic Resonance in Medicine, 77*, 0094–1103.
42. Schwan, H. P. (1957). Electrical properties of tissue and cell suspensions. *Advances in Biological and Medical Physics, 5*, 147–209.
43. Stoy, R. D., Foster, K. R., & Schwan, H. P. (1982). Dielectric properties of mammalian tissues from 0.1 to 100 MHz; a summary of recent data. *Physics in Medicine and Biology, 27*(4), 501–513.
44. Foster, K. R., Schepps, J. L., Stoy, R. D., & Schwan, H. P. (1979). Dielectric properties of brain tissues between 0.01 and 10 GHz. *Physics in Medicine and Biology, 24*, 1177–1187.
45. Smith, S. R., & Foster, K. R. (1985). Dielectric properties of low-water-content tissues. *Physics in Medicine and Biology, 30*, 965–973.
46. Kiricuta, I.-C., & Simplăceanu, V. (1975). Tissue water content and nuclear magnetic resonance in normal and tumor tissues. *Cancer Research, 35*(5), 1164–1167.
47. Wenger, C., Salvador, R., Basser, P. J., & Miranda, P. C. (2015). The electric field distribution in the brain during TTFields therapy and its dependence on tissue dielectric properties and anatomy : A computational study. *Physics in Medicine and Biology, 60*(18), 7339–7357.
48. van Lier, A. L., et al. (2011). Electrical conductivity imaging of brain tumours. In *Proceedings of the 19th Annual Meeting of ISMRM* (Vol. 19, p. 4464). Montréal.
49. Huhndorf, M., Stehning, C., Rohr, A., Helle, M., Katscher, U., & Jansen, O. (2013). Systematic brain tumor conductivity study with optimized EPT sequence and reconstruction algorithm. *Proceedings of the 21th Annual Meeting of ISMRM, Salt Lake City, 66*(2011), 3626.
50. Voigt, T. (2011). Imaging conductivity using electric properties tomography – initial clinical results in glioma patients. In *2011 XXXth URSI general assembly and scientific symposium* (pp. 1–4).